DOI: 10.1002/chem.201301965

Identification of Intermediates in Zeolite-Catalyzed Reactions by In Situ UV/Vis Microspectroscopy and a Complementary Set of Molecular Simulations

Karen Hemelsoet,*[a] Qingyun Qian,[b] Thierry De Meyer,[a] Kristof De Wispelaere,[a] Bart De Sterck,[a, c] Bert M. Weckhuysen,[b] Michel Waroquier,[a] and Veronique Van Speybroeck*[a]

Abstract: The optical absorption properties of (poly)aromatic hydrocarbons occluded in a nanoporous environment were investigated by theoretical and experimental methods. The carbonaceous species are an essential part of a working catalyst for the methanol-to-olefins (MTO) process. In situ UV/Vis microscopy measurements on methanol conversion over the acidic solid catalysts H-SAPO-34 and H-SSZ-13 revealed the growth of various broad absorption bands around 400, 480, and 580 nm. The cationic nature of the involved species was determined by interaction of ammonia with the methanol-treated samples. To determine which organic species contribute to the various bands, a systematic series of aromatics was analyzed by means of time-dependent density functional theory (TDDFT) calculations. Static gas-phase simulations revealed the influence of structurally different hydrocarbons on the absorption spectra, whereas the influence of the zeolitic framework was examined by using supramolecular models within a quantum mechanics/molecular mechanics framework. To fully understand the origin of the main absorption peaks, a molecular dynamics (MD) study on the organic species trapped in the inorganic host was essential. During such simulation the flexibility is fully taken into account and the effect on the UV/Vis spectra is determined by performing TDDFT calculations on various snapshots of the MD run. This procedure allows an energy absorption scale to be provided and the various absorption bands determined from in situ UV/Vis spectra to be assigned to structurally different species.

Keywords: density functional calculations · heterogeneous catalysis · molecular dynamics · UV/Vis spectroscopy · zeolites

Introduction

Obtaining detailed molecular-scale knowledge of carbonaceous compounds formed during heterogeneous catalysis remains a big challenge in modern spectroscopy.[1–3] Such information is nevertheless essential to elucidate the reaction mechanism of industrial processes producing chemicals and energy vectors. These complex processes are often based on the conversion of organic compounds over solid catalysts exhibiting a porous structure and an acid function. Hydrocarbon reaction intermediates formed in the conversion process may also grow into larger coke species that are retained in the pores and/or on the outer surface of the catalyst material.[4] To gain more insight into the exact nature and structure of the carbonaceous species, multimethod spectroscopic studies are nowadays the standard experimental approach, and UV/Vis measurements have become an indispensable part thereof.[3,5,6] In particular, the technique is highly sensitive to charged aromatic compounds, which give rise to numerous striking features in the visible range.[7] A major drawback is that in most cases only electronic transitions can be traced, whereas the rovibrational fine structure usually remains unsolved.[8] To fully interpret the experimental spectra, molecular modeling techniques are important, as they allow the electronic absorption of structurally different compounds to be simulated. Recent advances in first-principles molecular modeling techniques nowadays enable absorption spectra of relatively large compounds to be determined in a cost-efficient way.[9–11]

In this work, we aimed to assign bands in experimental in situ UV/Vis spectra taken during methanol conversion over chabazite catalysts to structurally different carbonaceous compounds by means of time-dependent density functional theory (TDDFT) combined with molecular dynamics (MD). The excitation energies of a systematic set of both neutral

[a] Prof. Dr. K. Hemelsoet, T. De Meyer, K. De Wispelaere, Dr. B. De Sterck, Prof. Dr. M. Waroquier, Prof. Dr. V. Van Speybroeck
Center for Molecular Modeling (CMM), Ghent University
Technologiepark 903, 9052 Zwijnaarde (Belgium)
QCMM-alliance, Ghent-Brussels (Belgium)
E-mail: karen.hemelsoet@ugent.be
veronique.vanspeybroeck@ugent.be

[b] Q. Qian, Prof. Dr. B. M. Weckhuysen
Inorganic Chemistry and Catalysis
Debye Institute for Nanomaterials Science
Utrecht University, Universiteitsweg 99
3584 CG, Utrecht (The Netherlands)

[c] Dr. B. De Sterck
Current address: Ineos Technologies, Scheldelaan 482
2040 Antwerp (Belgium)

Supporting information for this article is available on the WWW under http://dx.doi.org/10.1002/chem.201301965.

and charged (poly)aromatic hydrocarbons were computed in molecular environments with increasing complexity, that is, in vacuo, in a continuum solvent, and in a zeolitic material. Thus, the influence of the nanoporous environment on the electronic excitation characteristics of the carbonaceous compounds can be examined in detail. Some of us showed earlier that it is important to account for the flexibility of the UV/Vis-active compounds to get good agreement between theory and experiment.[12] Therefore, MD simulations were also performed for the gas-phase compounds and selected trapped organic species. The complementary set of methods used in this work allows the factors determining the typical fingerprints of cationic (poly)aromatic compounds in the UV/Vis spectra to be pinpointed on the basis of a combined static/molecular dynamics approach. Various factors may play an important role in the final assignment scale: 1) the level of theory used for the calculatation of the excitation spectra, 2) the zeolitic confinement effects, and 3) the flexibility of the organic compounds.

Our specific interest stems from the understanding of the methanol-to-olefins (MTO) process (Figure 1 a) occurring over the archetypal acidic solid catalysts H-ZSM-5 and H-SAPO-34.[13–15] Elucidation of the reaction mechanism has been the theme of a long debate, but there is now consensus on the hydrocarbon pool (HP) pathway, in which methanol is added to an organic scaffold present in the zeolite framework.[14,16–19] The MTO process has recently been reviewed.[20–22] The exact chemical structure of the HP species depends on the zeolite characteristics (composition, topology, acid strength) and the reaction conditions.[23–28] In H-ZSM-5 both alkenes and lower methylated aromatics are assumed to be active olefin-eliminating compounds,[29–35] whereas in H-SAPO-34 mainly higher methylated aromatics are held responsible for the catalytic activity.[36–41] The different catalysts also show different coking behavior. Details of the deactivation process in H-SAPO-34 have been reviewed by Chen et al.[42] Due to the complexity of the mechanism and the occurrence of various simultaneous reactions, the exact nature and structure of carbonaceous species formed during the MTO process remain unknown. In this light, molecular modeling has already been of indispensable value in unraveling various reaction mechanisms proposed for the MTO process.[31–34,43,44] Nowadays, theoretical methods have matured to the level at which enthalpy barriers[45] and reaction rates[46] of individual reaction steps occurring in zeolitic materials can be obtained with near-chemical accuracy.

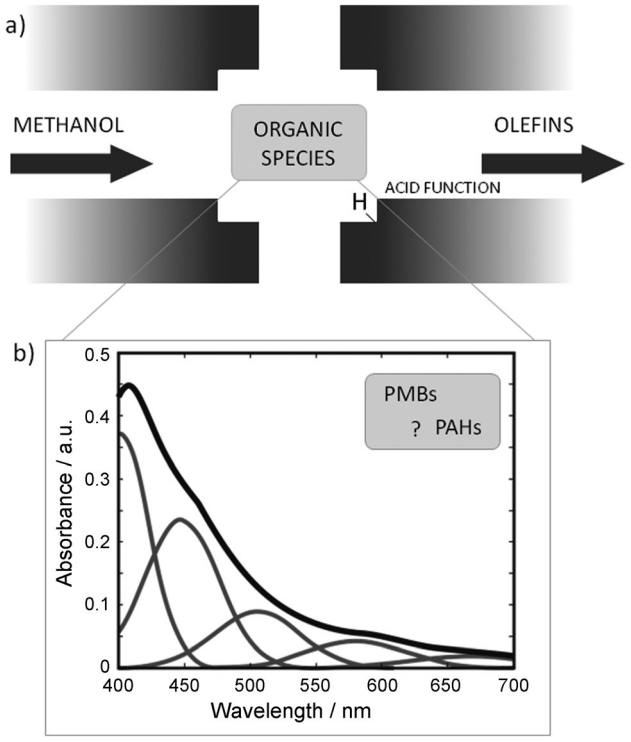

Figure 1. a) Schematic view of the hybrid organic/inorganic catalyst for MTO and b) schematic representation of a deconvoluted UV/Vis spectrum of methanol conversion over micrometer-sized crystals of H-SAPO-34.[47] During the conversion, a variety of PMBs and PAHs are present in the zeolitic pore.

Some of us used in situ UV/Vis combined with confocal fluorescence microspectroscopy to characterize coke species in H-ZSM-5[2,48–50] and H-SAPO-34.[2] In the latter, deactivation is due to large aromatic hydrocarbons trapped inside the spacious pores.[2] These aromatics are held responsible for pore blockage and hence deactivation of the SAPO-34 catalyst.[51] Dai et al. examined the catalytic performance of silicoaluminophosphate (SAPO) materials with different topologies, in particular SAPO-34, SAPO-41, SAPO-11, and SAPO-46, during MTO conversion and observed the formation of polyaromatic coke species using ^{1}H MAS NMR and in situ UV/Vis spectroscopy.[52,53] In particular, GC-MS analysis of the formed organic species revealed that for SAPO-34 mainly naphthalene is retained, for SAPO-41 and SAPO-11 tetramethylbenzenes, and for SAPO-46 the amounts of large aromatics are negligible.

One of the main problems with UV/Vis spectra is that their interpretation is complicated due to the occurrence of overlapping absorption bands. To obtain more information on the underlying carbonaceous species, the spectra can be deconvoluted, as illustrated in Figure 1 b.[47,48] In a combined theoretical/experimental study on methanol conversion over chabazite-type materials, we established a correlation between theoretical methylation activation barriers for the most active species and the formation–activation barriers of the underlying reaction intermediates deduced from UV/Vis microspectroscopy.[47] In correspondence with previous studies, absorption around 400 nm could be assigned to highly methylated benzenic cations. In particular, Bjørgen et al. assigned the band at 400 nm to the hexamethylbenzenium cation, which is a crucial MTO reaction intermediate.[39] This information will provide an important reference point for the theoretical simulations performed in the present work. The heptamethylbenzenium cation was recently explicitly observed under MTO conditions in DNL-6, a newly synthesized SAPO-type molecular sieve with large cavities.[54] Coupling of NMR to optical fiber based UV/Vis spectroscopy by Hunger et al. allowed the formation of

cyclic compounds and carbenium ions to be detected.[55] Dierksen and Grimme provided vibronically resolved spectra of polyaromatics, and reported absorption around 361 nm (theoretical value: 384 nm) in the case of anthracene.[8] Mores and co-workers associated absorption bands of UV/Vis spectra recorded during MTO over ZSM-5 with the following (cationic) carbonaceous deposits absorbing between 380 and 410 nm: single-ring aromatics; 425 and 475 nm: two- and three-ring aromatics; 565 and 635 nm; four- and five-ring aromatics; above 675 nm: polycondensed aromatics.[48] Also in the field of in situ spectroscopy, which is now regularly used to obtain insight into the detailed reaction mechanism,[56] molecular modeling may assist in interpreting the often complex spectra.

Time-dependent DFT[57–60] has nowadays emerged as the preferred theoretical tool to investigate reasonably large systems for which traditional methods based on wave functions are computationally infeasible. Although TDDFT is formally exact, practical implementation leads to approximations due to the nature of the exchange-correlation (xc) functional and the usually applied adiabatic approach. Nevertheless, reasonable accuracy is reached in the reproduction of excitation energies in fairly large molecules at very favorable computational cost; the typical error for the excitation energy lies in the range of 0.1–0.5 eV.[58,61–63] However, substantial errors may be expected for large π systems such as linear polyacenes when using standard functionals such as BP86 and B3LYP, since they show an incorrect asymptotic behavior for the xc potential. This problem was examined in detail by Grimme and Parac.[64] For an important class of excitations with ionic character unsystematic and strongly size dependent errors were obtained, and hence simple correction schemes were excluded. By including a long-range correction term to the functional, based on exact HF exchange at large distance, the performance of TDDFT could be resolved.[65–68] Excitation energies decrease monotonically with increasing size of the linear polycyclic aromatic hydrocarbons (PAHs). This seems not to be the case for their protonated counterparts, as experimentally demonstrated by Alata et al.,[69] who presented the first experimental observation of vibrationally resolved electronic spectra of protonated linear PAHs. For species with an even number of aromatic rings, the excited state shows a strong charge-transfer character leading to a large redshift of the transition.[69] Detailed knowledge of the electronic absorption properties of such PAHs, which encompass the HP reaction intermediates and coke precursors of the MTO process, as illustrated in Figure 1, is still a subject of research. Moreover, the computation of reliable electronic transitions for an entire supramolecular complex consisting of the nanoporous material and the hydrocarbon compound remains very challenging. Crucial host–guest interactions in zeolitic materials are typically studied by means of vibrational techniques such as IR spectroscopy, whereas the influence of such interactions on the electronic absorption properties is currently not well understood. Fois et al. investigated the dye fluorenone inside the nanochannels of zeolite L using TDDFT on finite clusters extracted from the periodically optimized structure.[70] The commonly used procedure to calculate UV/Vis spectra theoretically uses static electronic-structure calculations on a well-defined configuration of the potential-energy surface. However, the carbonaceous molecules encountered here show a certain degree of flexibility. Such effects may be fully accounted for by performing molecular dynamics (MD) simulations.[71] Molecular dynamics accurately describes the structural fluctuations during a small time interval and can generate a large series of different conformations which are used to obtain average excitation properties.[12,72,73] In practice, TDDFT simulations are performed on snapshots extracted from the MD trajectories.

The methodology used in this work allows the influence of both the zeolite confinement and the flexibility of the organic compounds on the theoretical excitation energies of the carbonaceous species occluded in the pores of the catalyst material to be fully quantified. The archetypal MTO catalysts H-SAPO-34 and H-SSZ-13 with chabazite (CHA) topology are taken as a case study. In situ UV/Vis experiments were performed, and interactions between ammonia and the coked samples provided insight into the charged nature of the formed species. A static and dynamic approach was assessed to simulate the excitation spectra, and finally an assignment scale based on the theoretical data is proposed.

Results and Discussion

In situ UV/Vis microspectroscopy: H-SAPO-34 and H-SSZ-13 zeolite crystals were placed on the heating stage of an in situ cell and exposed to a stream of methanol vapor at a reaction temperature of 509 K. We previously reported that broad, overlapping absorption bands grow around 400, 480, and 580 nm[2] and that a systematic deconvolution procedure can be performed to obtain more insight into the underlying reaction intermediates.[47] Four Gaussian bands, located at approximately 400, 450, 505, and 580 nm, were needed to properly reconstruct the experimental UV/Vis absorption spectra, while a band at 658 nm has a very small contribution to the overall shape, and a broad band at 700 nm was used to compensate the overall absorption due to coke formation or drift effect.[47] In the present study, we mainly focus on the time evolution of the Gaussian bands around 400, 450, and 505 nm. To reveal whether the organic intermediates reside in neutral or cationic form, the methanol-treated H-SAPO-34 and H-SSZ-13 samples were exposed to a stream of ammonia. NH_3 is believed to diffuse easily through the nanoporous structure due to its small size.

A selection of UV/Vis microspectra taken before (α, β) and after (γ, δ) ammonia dosing is given in Figure 2a and b. Figure 2c and d show the absorbance maxima of the Gaussian bands as a function of time on stream (TOS). The methanol flow was stopped after 1125 and 900 s in the case of H-SAPO-34 and H-SSZ-13, respectively (β in Figure 2). NH_3 dosing started shortly hereafter (γ in Figure 2) and immedi-

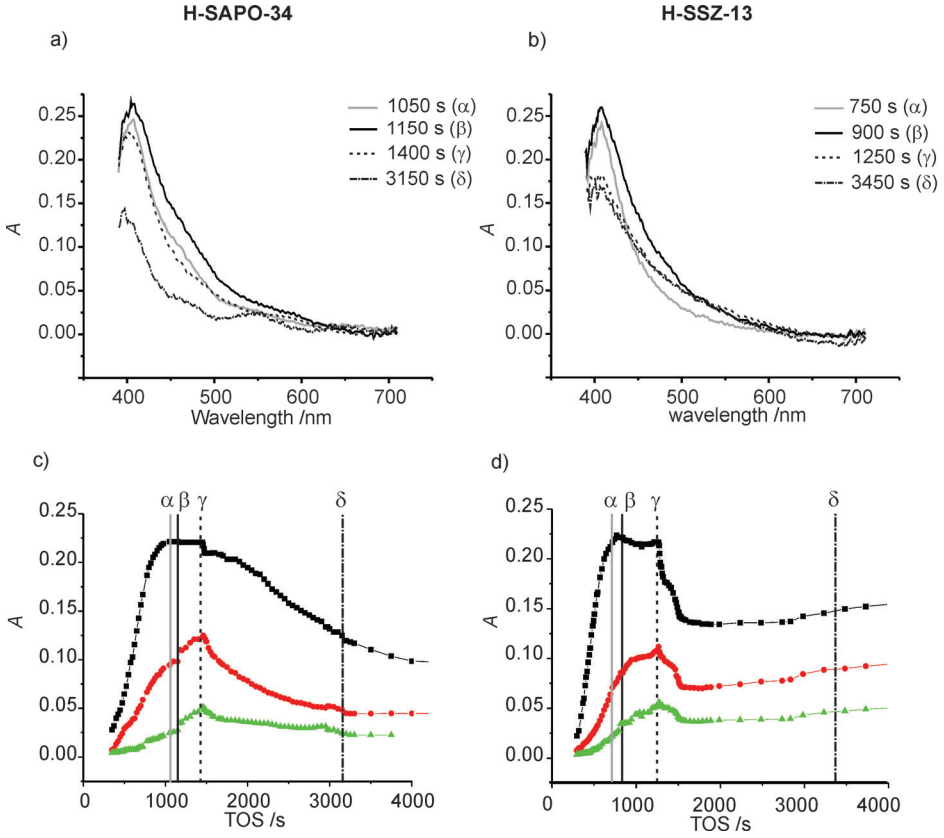

Figure 2. Selection of time-resolved UV/Vis spectra during MTO reaction at 509 K of the a) H-SAPO-34 and b) H-SSZ-13 crystals. c) and d) Time evolution of Gaussian bands (black squares, 400 nm; red circles, 449 nm; green triangles, 505 nm). At time β (1125 s for H-SAPO-34 and 900 s for H-SSZ-13) the methanol feed was stopped, and at time γ (1400 s for H-SAPO-34 and 1250 s for H-SSZ-13) the ammonia feed was started. We note that some spectra were rather challenging to fit and a maximum shift of 4 nm was allowed, similar to previous work.[2,47]

ately the bands started to drop. For the sake of comparison, the time evolution of the Gaussian bands for the reaction without ammonia is given in Figure S1 of the Supporting Information, in which a steady increase of the bands around 446 and 504 nm can be observed. On interaction with ammonia (Figure 2c and d), all bands decrease monotonically, that is, they are due to carbocations. However, the bands decrease at different rates. In particular, for H-SAPO-34 the Gaussian bands around 400 and 450 nm drop faster than the band at longer wavelength (505 nm). On the other hand, the bands drop much faster in H-SSZ-13, and a steady regime is noticed at 2000 s (Figure 2d). For this sample, outgassing was performed at about 2850 s, after which a small increase in the Gaussian bands was observed suggesting slow regeneration of aromatics (see δ in Figure 2 and Figure S2 of the Supporting Information). The differences between H-SAPO-34 and H-SSZ-13 may be due to differences in acidity and/or pore diffusion. We did not observe total erosion of the bands, as opposed to the situation in H-ZSM-5.[74] This might also be due to the different possibilities for pore diffusion in the MFI and CHA topologies.

The obtained results are in line with a recent investigation of Dai and co-workers, who combined the study of NH_3 with SAPO-34 samples used for MTO using UV/Vis and ^1H and ^{13}C high-speed MAS NMR.[75] Scheme 1 depicts possible interactions between ammonia and charged HP species and/or the zeolitic framework.

Ammonia is a relatively strong base and is a good candidate to deprotonate some trapped cationic species and form their neutral counterparts (Scheme 1a). The corresponding electronic changes are observable in the UV/Vis spectra.[39,74,75] In addition, Dai et al.[76] manifestly demonstrated using ^{13}C MAS NMR the formation of phenylammonium ions (Scheme 1b), and hence this route was also investigated by ab initio simulations. Moreover, protonation of the probe molecule by accessible Si(OH)Al sites leading to ammonium ions cannot be ruled out (Scheme 1c). The last-named effect does not lead to changes in the UV/Vis spectra; it only hampers the formation of protonated HP species, since fewer acidic protons are available. Gas-phase proton affinities (PAs) have been used previously to assess the stability of the formed carbocations; computed data of the species under investigation are given in Table S1 of the Supporting Information. Polymethylben-

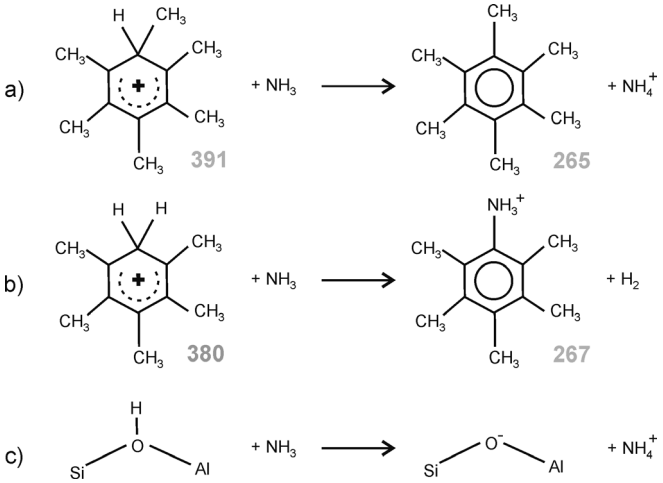

Scheme 1. Possible interactions between ammonia and charged HP species occluded in the CHA cage (a, b) and the acid site (c). Calculated excitation energies [nm] from MD simulations on the gas-phase compounds are also given (see text for more details).

zenes (PMBs) with a PA value higher than 820 kJ mol^{-1} have been shown to occur mostly in their protonated form inside H-Beta.[39] The results (Supporting Information, Table S1) indeed suggest that protonation of ammonia by the acidic framework protons may occur and that several aromatics can be deprotonated by NH_3. However, one must be careful when drawing conclusions based on these gas-phase data, as pointed out previously by Macht et al.[77]

TDDFT simulations of carbonaceous compounds: To obtain a comprehensive understanding of the observed UV/Vis spectra, a set of PMBs and PAHs was selected (Figure 3). The notations B_n, N_n, A_n, T_n, Ph_n and PYR_n stand for benzenic, naphthalenic, anthracenic, tetracenic, phenanthrenic, and pyrenic compounds with *n* methyl substituents. Due to the abundance of methanol, methylated carbocations are key intermediates in all mechanistic proposals for the MTO reaction (see Figure 3a) and hence their absorbance characteristics were also studied. Methylation can occur at various positions to give a charged carbonaceous compound X_{n+1}^+; the selected sites are indicated in Figure 3b. The optimized B3LYP/DGTZVP geometries of all gas-phase neutral compounds were found to be planar. Methylation can lead to small deviations from planarity; the benzenic species deviate slightly from planarity, whereas for the polyaromatics a maximum deviation of 17° is found in the case of the singly methylated tetracenic species. This behavior was previously shown to be relatively independent of the level of theory and of the inclusion of dispersion corrections.[78–80]

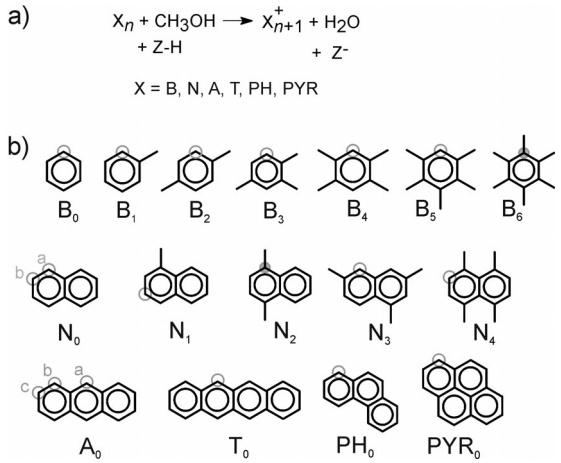

Figure 3. a) Schematic view of methylation reactions in MTO reaction mechanisms. Z represents the zeolite. b) Representation of all investigated neutral PMBs and PAHs, that is, all X_n species, where *n* is the number of methyl substituents and X stands for benzenic, naphthalenic, anthracenic, tetracenic, phenanthrenic, and pyrenic species. Cationic compounds resulting from methylation at the positions indicated by circles were also studied. Open and filled circles correspond to normal and *ipso* methylation, respectively.

Time-dependent DFT excitation spectra of the entire series of gas-phase compounds shown in Figure 3 were calculated. All excitations correspond to singlet $\pi \rightarrow \pi^*$ transitions. Table 1 lists the computed first excitation energies, and overall spectra are shown in Figure S4 of the Supporting Information.

Table 1. First excitation energies [nm] computed with TDDFT (B3LYP/DGTZVP).[a,b]

	Neutral compounds				Charged compounds		
	Static		MD		Static		MD
	In vacuo[a]	PCM	In vacuo		In vacuo[a]	PCM	In vacuo
B_0	229 (225)	229	240	B_1^+	305 (302)	312	323
B_1	234 (229)	234	245	B_2^+	322 (318)	330	342
B_2	240 (235)	241	251	B_3^+	344 (336)	350	368
B_3	241 (235)	241	253	B_4^+	357 (350)	364	378
B_4	242 (236)	243	256	B_5^+	370 (363)	378	394
B_5	246 (239)	246	260	B_6^+	361 (352)	369	391
B_6	249 (242)	249	265	B_7^+	360 (352)	367	385
N_0	284 (269)	287	307	N_{1a}^+	438 (382)	433	466
				N_{1b}^+	452 (423)	458	473
N_1	290 (276)	293	306	N_2^+	460 (429)	467	494
N_2	297 (275)	301	317	N_3^+	434 (376)	430	462
N_3	289 (283)	292	311	N_4^+	451 (394)	448	469
N_4	302 (283)	306	334	N_5^+	518 (473)	523	520
A_0	385 (349)	391	406	A_{1a}^+	445 (388)	445	480
				A_{1b}^+	644 (527)	633	691
				A_{1c}^+	655 (569)	654	682
T_0	506 (444)	516	531	T_1^+	616 (507)	614	653
PH_0	313 (292)	313	336	PH_1^+	522 (453)	523	559
PYR_0	338 (314)	346	358	PYR_1^+	618 (554)	618	623

[a] TDDFT CAM-B3LYP/DGTZVP results with B3LYP/DGTZVP optimized geometries are given in parentheses. [b] Static, In vacuo refers to TDDFT simulations in vacuo on gas-phase statically optimized structures; Static, PCM refers to TDDFT simulations including a PCM bulk solvent on gas-phase statically optimized structures; MD, In vacuo refers to the average excitation energy (TDDFT simulations in vacuo) with gas-phase structures extracted from an MD simulation.

Level-of-theory assessment for calculation of excitation spectra: First, the accuracy of the theoretical method must be validated. This was achieved by means of first excitation energies, which can be compared with data reported earlier.

For the neutral PAHs, all first excitations originate from typical HOMO→LUMO or from a mixture of HOMO−1→LUMO and HOMO→LUMO+1 excitations. These excitations are often referred to as L_a- and L_b-type states in the Platt nomenclature[81] and are a highly investigated research topic.[64–68,82] In particular, the nature of the L_a, that is, the HOMO→LUMO, excitation is a priori not well understood; to date there are indications of charge-transfer characteristics, and it has been reported that long range corrected functionals and double hybrids outperform standard GGA or hybrid functionals.[65–68] Therefore, for the series of linear acenes we also tested various functionals for the TDDFT computations, in particular BP86, B3LYP, B3P86, M06-2X, and CAM-B3LYP. The last-named method was previously shown to perform well for PAHs.[63,80,83,84] Figure 4a displays the main results; a detailed analysis is given in the Supporting Information. Figure 4a indeed shows that CAM-B3LYP leads to a substantial improvement for the first excitation of the longer acenes on comparing the theoretical results with

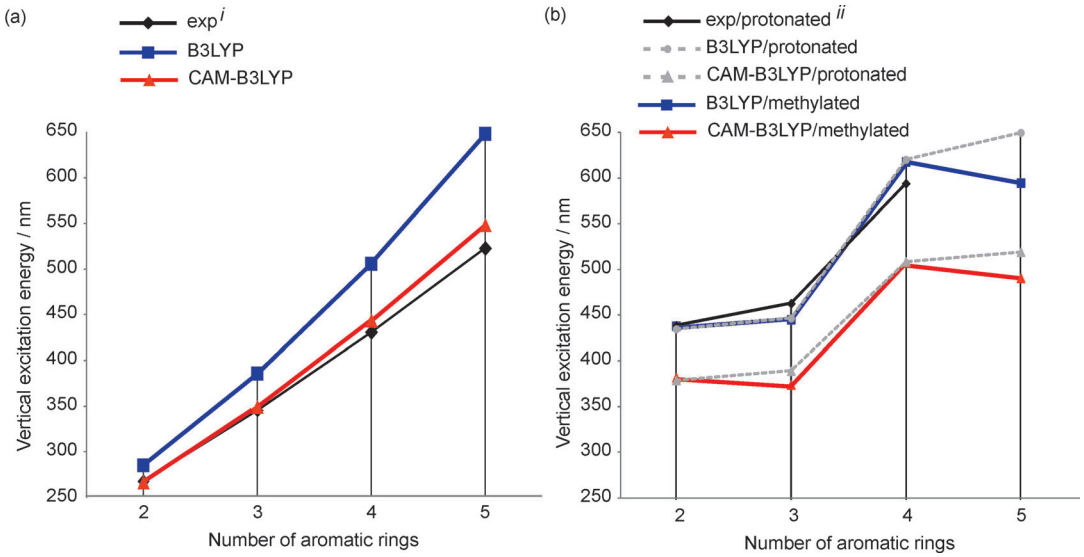

Figure 4. Comparison of experimental and theoretical (TDDFT) first excitation energies of a) linear condensed acenes and b) singly protonated or methylated linear condensed acenes as a function of system size. [i] Taken from ref. [64]. [ii] Adapted from ref. [69] (for details, see Supporting Information)

available experimental data. The M06-2X functional, which exhibits about the same amount of HF exchange as CAM-B3LYP at long distance, shows a very similar behavior. The maximal overestimation obtained for T_0 is reduced from 75 (for B3LYP) to 13 nm (for CAM-B3LYP), and thus a long range corrected functional with a substantial amount of HF exchange is preferred over GGA or hybrid functionals for the TDDFT-based description of HOMO→LUMO transitions in large linear acenes.[65]

In the case of the charged compounds, all first excitations correspond to a clear HOMO→LUMO transition, the computed oscillator strengths are much higher compared to those of their neutral counterparts. No systematic experimental data is available for charged methylated compounds, but Alata et al. obtained vibrationally resolved electronic spectra of isolated protonated PAHS, in particular naphthalene, anthracene, and tetracene, using neutral photofragment spectroscopy.[69] By using these compounds as a reference set, the performance of the B3LYP and CAM-B3LYP functionals was compared and, opposite to the series of neutral acenes, the shift between theoretical and experimental data was rather independent of system size (Figure 4b). Moreover, the B3LYP-based results for the charged compounds are in better agreement with the experimental reference data of Alata et al.

We are not only interested in the first excitations, since these often correspond to very low oscillator strengths (especially in case of the neutral aromatics), and therefore also investigated the influence of the level of theory on the overall spectra (see Figure S4 of the Supporting Information). The influence was found to be much smaller: comparison of B3LYP and CAM-B3LYP values for the maximal absorption peaks led to maximum shifts of 10 and 20 nm for neutral and charged series, respectively. These results suggest that the B3LYP functional is well suited to describe the overall excitation spectra of both neutral and charged (poly)aromatics.

The theoretical gas-phase simulations led to the following trend (see Figure S4 of the Supporting Information): for the series of neutral compounds, the maximal absorbance peak increases on average by 4 nm per methyl group, whereas for the X_0 series an increase of 30 nm is found on adding more aromatic rings in a linear fashion. Removal of the degeneracy of the energy levels on methylation of the aromatic backbone gives rise to a large redshift, to such an extent that also for benzenic species spectral components appear in the visible region (Figure 5). This observation is in agreement with previous studies on protonated (closed-shell) PAHs.[7,69,85] For the B_n^+ series the first excitation energy increases by approximately 16 nm per methyl group up to five substituents, after which it remains virtually identical for B_6^+ and B_7^+. The redshift induced by methylation can critically depend on the specific site where methylation takes place. This is especially the case in anthracenic compounds, for which the excitation energies can even differ by 210 nm (most stable compound A_{1a}^+ versus A_{1c}^+). The range in which the excitation energies lie is not always decisive for distinguishing between PAHs: N_{1a}^+ and A_{1a}^+ differ by only 7 nm, and hence singly methylated bi- or tricyclic compounds are indistinguishable in the experimental UV/Vis spectra. Figure 5 shows the computed first excitations, and it can be concluded that, in line with the experimental observations, mainly charged compounds show electronic absorbance in the visible region.

However, the computed excitation energies of the higher methylated benzenic species in the gas phase (e.g., 361 nm for B_6^+, see Table 1) are still substantially shifted from the experimental band position of 400 nm measured in H-SAPO-34. To assess the influence of a bulk solvent on the first vertical excitation energies, additional TDDFT calcula-

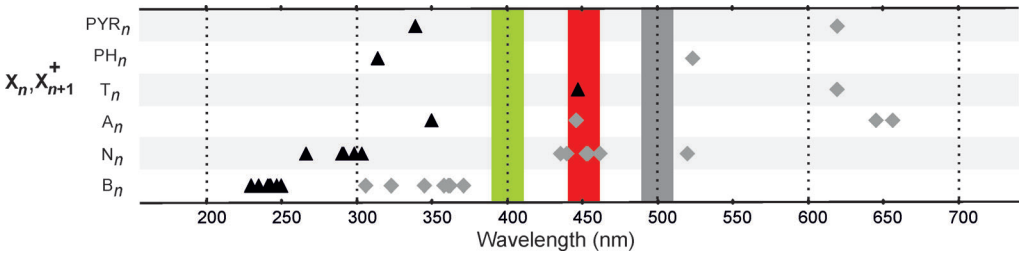

Figure 5. Theoretical first excitation energies [nm] of all optimized neutral (black triangles, calculated with TDDFT CAM-B3LYP) and charged (gray diamonds, calculated with TDDFT B3LYP) gas-phase compounds. The Gaussian bands around 400, 450, and 500 nm used in the experimental deconvolution procedure are indicated in green, red, and gray, respectively.

tions were performed in which the species were embedded in a continuum with fixed dielectric constant (the value of cyclohexane was used) with optimized geometries obtained in vacuo (column PCM in Table 1). The effect is negligible for the neutral compounds and somewhat larger for the charged compounds (maximal shift of 10 nm for A_{1b}^+). The theoretical excitation energy of B_6^+ now amounts to 369 nm, which is still too far from the 400 nm band measured experimentally. This is a clear indication that the effects taken into account up to now are insufficient to describe the measured optical absorption bands in a zeolitic environment.

Zeolitic confinement effects: To account for zeolite confinement and its influence on the calculated excitation properties, TDDFT simulations were performed on supramolecular systems with the species occluded in the chabazite pore. For this analysis, only the charged species were investigated and four-ring aromatics were omitted, since they are too large to be formed in the nanoporous cage. The computed first excitation energies of the carbocations in SAPO-34 are summarized in Table S4 of the Supporting Information. The influence is rather small: the zeolitic environment is responsible for a nonsystematic shift of 10 nm on average. Figure 6 illustrates that this effect may be due to geometrical deformation or mixing with zeolite orbitals.

In the cage of a zeolite the carbonaceous species exhibits a deformed structure so that the entire supramolecular system is in its energetically most favorable state. For some

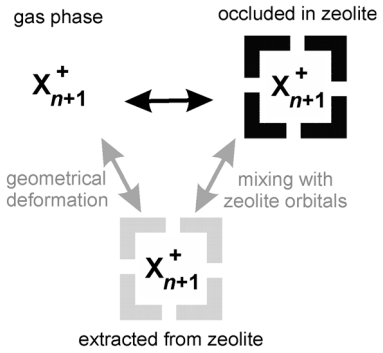

Figure 6. Schematic view of possible effects on excitation energies of carbonaceous compounds X_{n+1}^+ in gas-phase and supramolecular situations.

compounds this geometrical deformation can be very significant, as shown in Figure 7, which shows the calculated difference in electronic excitation energy between the optimized and deformed structures in vacuo versus the deformation energy. Deformation energies (see also Table S5 of the Supporting Information) of the benzenic species are relatively low, as could be expected due to the limited geometrical relaxation that these compounds can undergo. The resulting shifts in first excitation energy are also small (1–15 nm, see the gray zone in Figure 7). The longer the chain of rings, the higher the flexibility of the compounds and the geometrical deformation that can take place. These larger PAHs show substantially larger shifts: about 20-40 nm for the heavily deformed N_4^+, N_5^+, PH_1^+, A_{1b}^+, and A_{1c}^+ species (see Figure 7). The calculated results again illustrate the importance of the methylation site: in case of the anthracenium ions, methylation at the central ring leads to the most favorable situation, whereas the other structures A_{1b}^+ and A_{1c}^+ show deformation energies of 111 and 139 kJ mol^{-1}, respectively, which are extremely high.

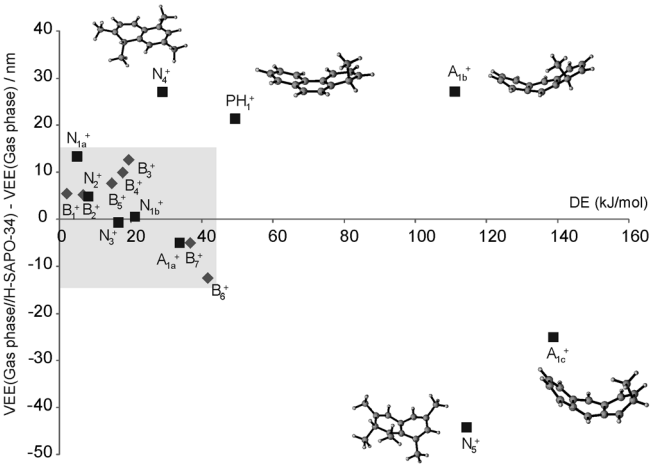

Figure 7. Calculated differences in first excitation energies [nm] of the deformed gas-phase compounds compared to the optimized structures as a function of deformation energy [kJ mol^{-1}]. The benzenic series is indicated by dark gray diamonds, and the PAH compounds by black squares.

Next, we compare the absorption spectra of the supramolecular systems with those of the deformed HP compounds extracted from the zeolite to assess the influence of

orbital mixing, as also schematically indicated in Figure 6. For the B_n^+ series, the first excitations are all shifted to higher values by an average of 12 nm, whereas for the PAHs the behavior is less systematic. Figure 8 illustrates the overall absorption spectrum for B_7^+ and N_4^+, which were investigated in SAPO-34 and its isostructural counterpart SSZ-13. For the heptamethylbenzenium ion the shift due to all these effects is almost nonexistent. For the bicyclic species, the zeolite-confinement effect is more prominent and leads to significantly larger shifts. Figure 8 also depicts molecular orbitals involved in the electronic excitations, which reveal that, for the supramolecular systems, mixing with zeolitic orbitals is sometimes observed. For the benzenic species, lower-lying π orbitals, delocalized over B_7^+ and the zeolite framework, participate in the excitation. A similar delocalization of the orbital surface is observed in the case of N_4^+.

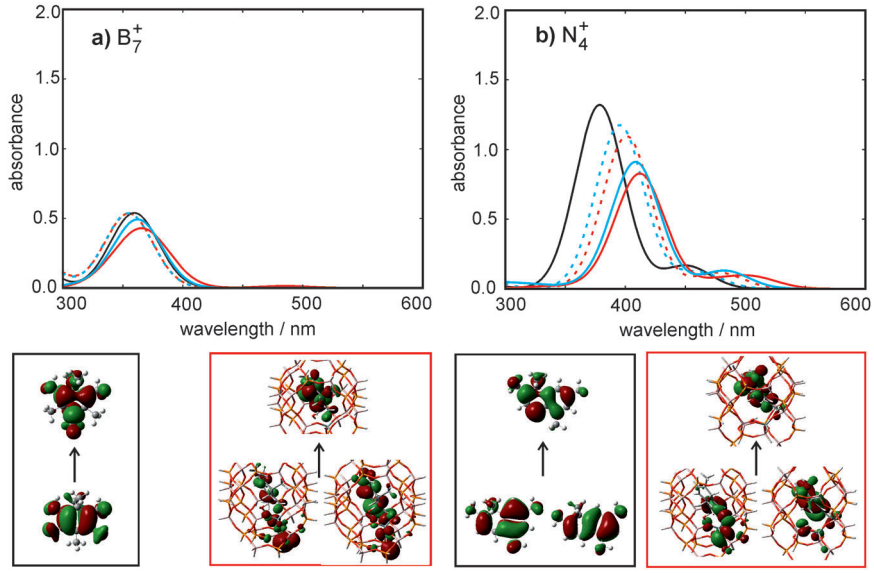

Figure 8. Simulated absorption spectra of a) B_7^+ and b) N_4^+ in different molecular environments: optimized structure in vacuo (full black line), deformed structure in vacuo extracted from geometry optimization of the supramolecular system (dashed lines), and the whole supramolecular system (full colored lines). Red lines correspond to SAPO-34, and blue lines to SSZ-13. The lower panels display isosurfaces (isovalue 0.02) of molecular orbitals involved in the electronic transitions; the black box corresponds to the system in vacuo, and the red box to the SAPO-34 supramolecular system.

A larger effect is found for this larger compound (see Figure 8). This analysis shows that differences between the electronic transitions of gas-phase and supramolecular compounds result from a complex, nonsystematic combination of geometrical deformation due to zeolitic confinement on the one hand and mixing of the orbitals of the carbonaceous compounds with those of the zeolitic framework on the other (Figure 8).

Flexibility of the organic compounds: *MD simulations*: Thus far, the theoretical analysis was based on static computations in which only one point on the potential-energy surface was taken into consideration. It has been shown by some of us that, for adequate simulation of UV/Vis spectra of azo dyes, it was of utmost importance to take into account the flexibility of the target compounds.[12] We therefore performed for all gas-phase compounds MD simulations at 600 K to sample the potential-energy surface and generate a large set of deformed structures which mimic the flexibility of the species at elevated temperatures. For the selected compounds B_7^+ and N_4^+ the dynamics included the zeolite framework. After proper equilibration, a production run was carried out. Subsequently, 100 snapshots were extracted, a static TDDFT calculation was then performed on each of them, and corresponding averages were taken. Figure 9 shows the influence of the MD approach for some neutral species and their charged counterparts. Overall, the shape of the spectra remains unaltered, but slight broadening of the absorption bands is found due to the inclusion of a large number of slightly deformed geometries. Figure 10a clearly shows only a small shift for the neutral compounds, whereas the influence of flexibility is more pronounced for the charged species (see Figure 9b). From the MD trajectories it can be concluded that small geometrical changes, and in particular deformations from planarity of the aromatic backbone, are responsible for the changes in the electronic excitation spectra. Out-of-plane movement of the sp^3-hybridized carbon atom in the carbocations is also noticeable.

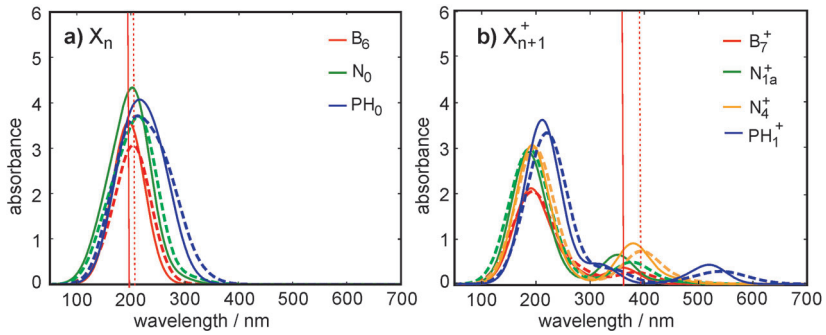

Figure 9. Comparison of the static (solid lines) and dynamic (dashed lines) approach for the computation of excitation spectra (wavelength range between 0 and 700 nm) for selected a) neutral and b) charged species in vacuo. Vertical lines correspond to the position of maximal absorbance for the B_6 and B_7^+ species.

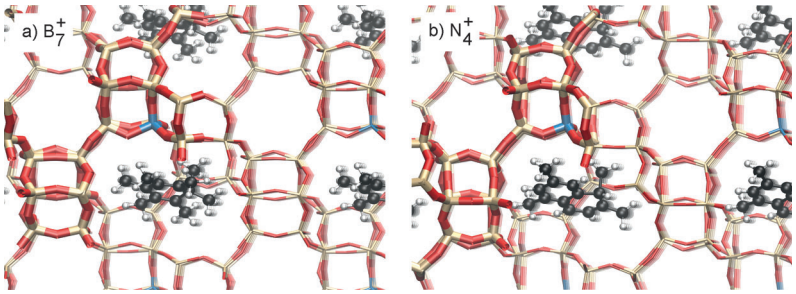

Figure 10. Periodic SSZ-13 structure with B_7^+ (a) or N_4^+ (b) used for the MD simulations.

The MD predictions of the first excitation wavelengths are included in Table 1 (column MD). In all cases, they show a significant bathochromic shift with respect to the static result. For the neutral series, this shift is about 20 nm, whereas for the cationic compounds it is approximately 30 nm. The MD values for the heavily methylated benzenium ions B_6^+ and B_7^+ are now 391 and 385 nm (see the dashed vertical line in Figure 9b), which are very close to the experimental absorption band of 400 nm. These results indicate that it is crucial to account for the flexibility of the carbonaceous species to get good agreement between theory and experiment, and that MD is an appropriate tool to do this. For the experimental reactions with ammonia, the MD-derived excitation energies are also included in Scheme 1. The deprotonated B_6 species and the pentamethylated phenylammonium ion absorb at 265 nm, and both routes (Scheme 1a and b) can explain the experimentally observed decrease of the 400 nm band on dosing NH_3.

Finally, we investigated the influence of the CHA cage on the MD simulations. MD runs at 600 K with the B_7^+ and N_4^+ compounds occluded in the CHA cage were calculated by using the periodic structures depicted in Figure 10. Subsequently, TDDFT computations were performed on snapshots taken from the MD runs, considering only the deformed HP species. The averaged excitation energy for B_7^+ of 384 nm is very similar to the averaged gas-phase MD value of 385 nm (see Table 1). This indicates that the CHA pore does not impose additional constraints on the heavily methylated benzenic species, in line with the observations made in the static calculation. In the case of N_4^+, the average MD value of 481 nm is substantially higher than the gas-phase MD average of 469 nm (see Table 1), and very similar to the static result for N_4^+ in the H-SSZ-13 large cluster (the HOMO and HOMO−1 to LUMO transition energy is 483 nm). This observation suggests an influence of the acidity of the catalyst material; a detailed investigation of this behavior is, however, outside the scope of the present work.

Assignment scale: In summary, the extensive theoretical study on absorption maxima of possible intermediates during an MTO process makes it possible to assign peaks in the experimental UV/Vis spectra. The assignment of the peaks is based on the theoretical data originating from the MD runs performed on the gas-phase species. The assignment scale for the carbocations is given in Figure 11, and the computed spectra are also shown in Figure S5 of the Supporting Information. Most of the single-ring aromatic cations contribute to the 400 nm band. Bicyclic species show broader absorption bands extending to 450 nm. Other bicyclic compounds, for example, the heavily methylated N_5^+, show absorbance around 500 nm. The phenanthrenic species show high absorbance at longer wavelengths, in particular

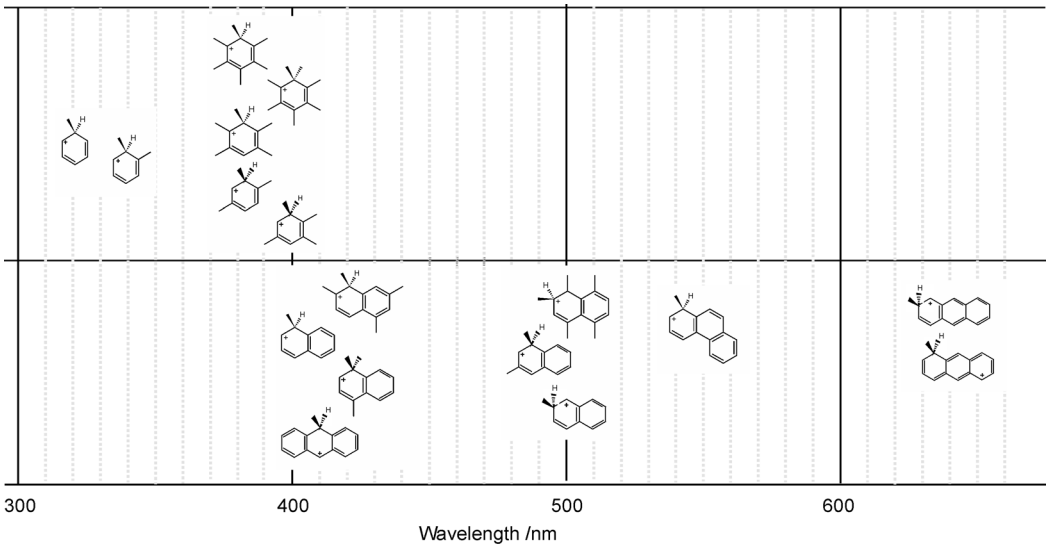

Figure 11. First vertical excitation energies [nm] of charged HP compounds in vacuo, computed by using MD combined with TDDFT B3LYP/DGTZV calculations on extracted snapshots.

around 540 nm. The anthracenic species A_{1b}^+ and A_{1c}^+ absorb above 650 nm. However, these species are energetically much less favorable than their A_{1a}^+ counterpart, which absorbs around 400 nm. It is therefore not expected that the former two compounds are important intermediates in the reaction. According to our theoretical simulations (see Table 1), no neutral compounds of our test set absorb above 600 nm. We also note that this assignment scale shows subtle differences from our previously proposed scale given in ref. [47], which only reported results obtained from static simulations.

Conclusion

We have presented theoretical excitation energies of a series of neutral and charged (poly)aromatic hydrocarbons in different molecular environments. These data provide insight at the molecular level into reaction intermediates responsible for absorption bands in experimental UV/Vis spectra. Methanol conversion over chabazite catalysts was examined and the bands in the experimental optical absorption spectra were obtained through in situ UV/Vis microspectroscopic measurements. The cationic nature of the species responsible for absorption around 400, 450, and in part 500 nm has been established by interaction of ammonia with the methanol-treated samples. On the basis of calculated excitation energies, the origin of this absorption has been attributed to structurally different (poly)aromatic compounds. We have shown that the use of static TDDFT computations on gas-phase compounds is insufficiently accurate and that one must be careful when incorporating the zeolite framework in the TDDFT simulation due to orbital mixing. We have demonstrated that molecular dynamics simulations are necessary to take into account geometrical deformations of the carbonaceous compounds, and this leads to broad absorption bands and average excitation values in excellent agreement with experimental data. Heavily methylated benzenium ions absorb around 400 nm, but singly methylated bi- and tricyclic species also absorb at this wavelength. Naphthalenium ions containing up to four methyl substituents are responsible for absorption around 450 nm, and the more heavily methylated bicyclic species as well as tricyclic compounds contribute to the 500 nm band.

Experimental Section

In situ experiments: The as-synthesized H-SAPO-34 and H-SSZ-13 crystals had sizes of $50\times50\times50$ and $40\times40\times40$ μm, respectively. Their synthesis is reported elsewhere.[86–88] The (Al+P)/Si and Si/Al ratios were 4.9 and 17.7, respectively. The crystals were placed on the heating stage of an in situ cell (Linkam FT-IR 600) equipped with a temperature controller (Linkam TMS 93). The calcined crystals were first heated to 673 K at 15 K min^{-1}, then heated to 823 K at 5 K min^{-1}, and held at this temperature for 1 h under O_2 atmosphere. Subsequently, the crystals were exposed to a stream of methanol vapor/N_2 (50 mL min^{-1}) at a reaction temperature of 509 K. The UV/Vis microspectroscopic measurements were performed under an Olympus BX41 upright microscope with a 50×0.5 N.A. high working distance microscope objective lens. A 75 W tungsten lamp was used for illumination. In addition, the microscope has a 50/50 double viewpoint tube, which accommodates a CCD video camera (ColorView IIIu, Soft Imaging System GmbH) and an optical fiber mount. A 200 μm core fiber connects the microscope to a CCD UV/Vis spectrometer (AvaSpec-2048TEC, Avantes BV).

Methanol feeding was stopped when no further increase in the absorption band around 400 nm was observed (1125 s for H-SAPO-34 and 900 s for H-SSZ-13). Shortly hereafter, 1% NH_3 in N_2 was introduced into the system at a flow rate of approximately 20 mL min^{-1}. In the case of H-SSZ-13, NH_3/N_2 was switched to pure N_2 flow (70 mL min^{-1}) after 2850 s when the intensities in visible region no longer declined.

Computational details: First-principles static calculations were performed with the Gaussian 03[89] and Gaussian 09[90] software packages. The equilibrium geometries of the ground states of the gas-phase compounds were determined at the B3LYP/DGTZVP level of theory.[91,92] The catalytic environment was modeled by using large (44T) finite zeolite clusters cut out of the crystallographic structure and containing one acid site per cage. The supramolecular geometries were optimized by using the multilayered ONIOM(B3LYP/DGTZVP:MNDO) method; the high level is composed of a 6T region, representing the central spacious cage of the chabazite topology (see also refs. [47,93,94]). The clusters are depicted in Figure S6 of the Supporting Information. A vibrational analysis at the level of theory of the geometry optimization confirmed the true nature of the stationary points. The outer hydrogen atoms of the cluster were constrained in space to prevent nonphysical deformations due to neglecting the full molecular environment. It has previously been shown that, from a technical point of view, the localization of transition states and interpretation of the normal modes is substantially simpler in a cluster approach than in a periodic approach.[95,96] In addition, we also reported that large cluster models provide accurate adsorption enthalpies when dispersion contributions are properly taken into account.[97]

Vertical electronic excitation energies were determined by using TDDFT at the B3LYP/DGTZVP level of theory. Additional BP86, B3P86, M06-2X, and CAM-B3LYP single-point TDDFT computations were performed. The CAM-B3LYP functional is a long range corrected functional with improved performance for delocalized systems,[98] and its performance is now tested for aromatic species bearing a positive charge. TDDFT computations with inclusion of a continuum solvent were also performed by using the polarizable continuum model (PCM)[99] with the solvent molecule density (SMD)[100] parameter set, as implemented in Gaussian 09.

Molecular dynamics (MD) simulations were carried out both on gas-phase hydrocarbons and selected carbocations entrapped in a chabazite cage by using the CP2K software package.[101] All DFT calculations are performed with the Gaussian and plane waves (GPW) method,[102] by using a TZVP basis set with GTH pseudopotentials[103,104] and the BLYP functional, to which empirical dispersion corrections were added according to the DFT-D3 Scheme of Grimme.[105] The gas-phase and zeolite MD runs were conducted in the canonical (NVT) ensemble at 600 K with time steps of 1 and 0.5 fs, respectively. A chain of five Nosé–Hoover thermostats was used to control the temperature. During MD runs in which the zeolite environment was taken into account, the volume of the periodic simulation cell was kept fixed. The cell parameters were obtained from a cell optimization and correspond to $a=13.870$, $b=13.886$, $c=14.867$ Å, $\alpha=89.89$, $\beta=90.08$, and $\gamma=118.36°$. The periodically repeated unit cell, as obtained from the IZA database, contains 36 tetrahedral units: 1 AlO_4 and 35 SiO_4 units. The use of this large unit cell avoids undesired interactions between the images of the hydrocarbon molecules. After equilibration, total simulation times of 50 and 3 ps were used for analysis of the gas-phase and zeolite MD runs, respectively, with the statistical analysis toolkit MD-tracks[106] and for the calculation of the "dynamic" UV/Vis spectra. These spectra were obtained by taking 100 snapshots (every 500 steps for the gas-phase simulations and every 60 steps for the zeolite simulations), on which separate TDDFT calculations were performed. Finally, all of the generated spectra were summed up and divided by the total number of snapshots (in this case, 100) to gain an aver-

aged spectrum based on the dynamics simulations. The calculated transition excitation energies are reported in wavelength units to allow a clear comparison with available experimental data.

Acknowledgements

We thank the Fund for Scientific Research - Flanders (FWO), the Research Board of Ghent University, and BELSPO in the frame of IAP/7/05. Funding was also received from the European Research Council under the European Community's Seventh Framework Programme [FP7(2007-2013) ERC grant agreement number 240483]. Computational resources and services used in this work were provided by Ghent University. This work was also supported by the Dutch National Science Foundation (NWO-CW VICI and TOP subsidies to B.M.W.) and the National Research School Combination Catalysis (NRSC-C). Prof. J. Kornatowski (Max Planck Institue of Mulheim) and E. Eilertsen (University of Oslo) are acknowledged for providing the zeolite crystals.

[1] M. Guisnet, *Appl. Catal. A* **2001**, *212*, 83–96.
[2] D. Mores, E. Stavitski, M. H. F. Kox, J. Kornatowski, U. Olsbye, B. M. Weckhuysen, *Chem. Eur. J.* **2008**, *14*, 11320–11327.
[3] I. Kiricsi, H. Forster, G. Tasi, J. B. Nagy, *Chem. Rev.* **1999**, *99*, 2085–2114.
[4] M. Guisnet, J. P. Gilson in *Zeolites for Cleaner Technologies, Catal. Sci. Ser. Vol. 3*, Imperial College Press, London, **2002**.
[5] M. Hunger, J. Weitkamp, *Angew. Chem.* **2001**, *113*, 3040–3059; *Angew. Chem. Int. Ed.* **2001**, *40*, 2954–2971.
[6] R. A. Schoonheydt, *Chem. Soc. Rev.* **2010**, *39*, 5051–5066.
[7] A. Pathak, P. J. Sarre, *Mon. Not. R. Astron. Soc.* **2008**, *391*, L10–L14.
[8] M. Dierksen, S. Grimme, *J. Chem. Phys.* **2004**, *120*, 3544–3554.
[9] L. González, D. Escudero, L. Serrano-Andres, *ChemPhysChem* **2012**, *13*, 28–51.
[10] F. Plasser, M. Barbatti, A. J. A. Aquino, H. Lischka, *Theor. Chem. Acc.* **2012**, *131*, 1073.
[11] C. Adamo, D. Jacquemin, *Chem. Soc. Rev.* **2013**, *42*, 845–856.
[12] T. De Meyer, K. Hemelsoet, L. Van der Schueren, E. Pauwels, K. De Clerck, V. Van Speybroeck, *Chem. Eur. J.* **2012**, *18*, 8120–8129.
[13] M. Stöcker, *Microporous Mesoporous Mater.* **1999**, *29*, 3–48.
[14] J. F. Haw, W. Song, D. M. Marcus, J. B. Nicholas, *Acc. Chem. Res.* **2003**, *36*, 317–326.
[15] B. V. Vora, T. L. Marker, P. T. Barger, H. R. Nilsen, S. Kvisle, T. Fuglerud, *Stud. Surf. Sci. Catal.* **1997**, *107*, 87–98.
[16] I. M. Dahl, S. Kolboe, *Catal. Lett.* **1993**, *20*, 329–336.
[17] I. M. Dahl, S. Kolboe, *J. Catal.* **1994**, *149*, 458–464.
[18] I. M. Dahl, S. Kolboe, *J. Catal.* **1996**, *161*, 304–309.
[19] W. G. Song, D. M. Marcus, H. Fu, J. O. Ehresmann, J. F. Haw, *J. Am. Chem. Soc.* **2002**, *124*, 3844–3845.
[20] U. Olsbye, S. Svelle, M. Bjorgen, P. Beato, T. V. W. Janssens, F. Joensen, S. Bordiga, K. P. Lillerud, *Angew. Chem. Int. Ed.* **2012**, *51*, 5810–5831.
[21] S. Ilias, A. Bhan, *ACS Catal.* **2013**, *3*, 18–21.
[22] K. Hemelsoet, J. Van der Mynsbrugge, K. De Wispelaere, M. Waroquier, V. Van Speybroeck, *ChemPhysChem* **2013**, *14*, 1526–1545.
[23] F. Zhou, P. Tian, Z. Liu, G. Liu, F. Chang, J. Li, *Chin. J. Catal.* **2007**, *28*, 817–822.
[24] L. Zhang, C. Yang, X. Meng, B. Xie, L. Wang, L. Ren, S. Ma, F.-S. Xiao, *Chem. Mater.* **2010**, *22*, 3099–3107.
[25] Y. Kumita, J. Gascon, E. Stavitski, J. a. Moulijn, F. Kapteijn, *Appl. Catal. A* **2011**, *391*, 234–243.
[26] S. Teketel, S. Svelle, K. P. Lillerud, U. Olsbye, *ChemCatChem* **2009**, *1*, 78–81.
[27] S. Teketel, U. Olsbye, K. P. Lillerud, P. Beato, S. Svelle, *Microporous Mesoporous Mater.* **2010**, *136*, 33–41.
[28] Z. Cui, Q. Liu, Z. Ma, S. Bian, W. Song, *J. Catal.* **2008**, *258*, 83–86.
[29] R. M. Dessau, *J. Catal.* **1986**, *99*, 111–116.
[30] M. Bjørgen, F. Joensen, K.-P. Lillerud, U. Olsbye, S. Svelle, *Catal. Today* **2009**, *142*, 90–97.
[31] D. Lesthaeghe, B. De Sterck, V. Van Speybroeck, G. B. Marin, M. Waroquier, *Angew. Chem.* **2007**, *119*, 1333–1336; *Angew. Chem. Int. Ed.* **2007**, *46*, 1311–1314.
[32] D. M. McCann, D. Lesthaeghe, P. W. Kletnieks, D. R. Guenther, M. J. Hayman, V. Van Speybroeck, M. Waroquier, J. F. Haw, *Angew. Chem.* **2008**, *120*, 5257–5260; *Angew. Chem. Int. Ed.* **2008**, *47*, 5179–5182.
[33] D. Lesthaeghe, A. Horre, M. Waroquier, G. B. Marin, V. Van Speybroeck, *Chem. Eur. J.* **2009**, *15*, 10803–10808.
[34] D. Lesthaeghe, J. Van der Mynsbrugge, M. Vandichel, M. Waroquier, V. Van Speybroeck, *ChemCatChem* **2011**, *3*, 208–212.
[35] S. Svelle, F. Joensen, J. Nerlov, U. Olsbye, K.-P. Lillerud, S. Kolboe, M. Bjorgen, *J. Am. Chem. Soc.* **2006**, *128*, 14770–14771.
[36] W. Song, J. F. Haw, J. B. Nicholas, C. S. Heneghan, *J. Am. Chem. Soc.* **2000**, *122*, 10726–10727.
[37] B. Arstad, S. Kolboe, *J. Am. Chem. Soc.* **2001**, *123*, 8137–8138.
[38] B. Arstad, S. Kolboe, *Catal. Lett.* **2001**, *71*, 209–212.
[39] M. Bjørgen, F. Bonino, S. Kolboe, K.-P. Lillerud, A. Zecchina, S. Bordiga, *J. Am. Chem. Soc.* **2003**, *125*, 15863–15868.
[40] M. Bjorgen, U. Olsbye, D. Petersen, S. Kolboe, *J. Catal.* **2004**, *221*, 1–10.
[41] J. F. Haw, D. M. Marcus, *Top. Catal.* **2005**, *34*, 41–48.
[42] D. Chen, K. Moljord, A. Holmen, *Microporous Mesoporous Mater.* **2012**, *164*, 239–250.
[43] D. Lesthaeghe, V. Van Speybroeck, G. B. Marin, M. Waroquier, *Angew. Chem.* **2006**, *118*, 1746–1751; *Angew. Chem. Int. Ed.* **2006**, *45*, 1714–1719.
[44] K. De Wispelaere, K. Hemelsoet, M. Waroquier, V. Van Speybroeck, *J. Catal.* **2013**, *305*, 76–80.
[45] S. Svelle, C. Tuma, X. Rozanska, T. Kerber, J. Sauer, *J. Am. Chem. Soc.* **2009**, *131*, 816–825.
[46] V. Van Speybroeck, J. Van der Mynsbrugge, M. Vandichel, K. Hemelsoet, D. Lesthaeghe, A. Ghysels, G. B. Marin, M. Waroquier, *J. Am. Chem. Soc.* **2011**, *133*, 888–899.
[47] V. Van Speybroeck, K. Hemelsoet, K. De Wispelaere, Q. Qian, J. Van der Mynsbrugge, B. De Sterck, B. M. Weckhuysen, M. Waroquier, *ChemCatChem* **2013**, *5*, 173–184.
[48] D. Mores, J. Kornatowski, U. Olsbye, B. M. Weckhuysen, *Chem. Eur. J.* **2011**, *17*, 2874–2884.
[49] D. Mores, E. Stavitski, S. P. Verkleij, A. Lombard, A. Cabiac, L. Rouleau, J. Patarin, A. Simon-Masseron, B. M. Weckhuysen, *Phys. Chem. Chem. Phys.* **2011**, *13*, 15985–15994.
[50] J. P. Hofmann, D. Mores, L. R. Aramburo, S. Teketel, M. Rohnke, J. Janek, U. Olsbye, B. M. Weckhuysen, *Chem. Eur. J.* **2013**, *19*, 8533–8542.
[51] B. P. C. Hereijgers, F. Bleken, M. H. Nilsen, S. Svelle, K.-P. Lillerud, M. Bjorgen, B. M. Weckhuysen, U. Olsbye, *J. Catal.* **2009**, *264*, 77–87.
[52] W. Dai, X. Wang, G. Wu, N. Guan, M. Hunger, L. Li, *ACS Catal.* **2011**, *1*, 292–299.
[53] W. Dai, N. Li, L. Li, N. Guan, M. Hunger, *Catal. Commun.* **2011**, *16*, 124–127.
[54] J. Li, Y. Wei, J. Chen, P. Tian, X. Su, S. Xu, Y. Qi, Q. Wang, Y. Zhou, Y. He, Z. Liu, *J. Am. Chem. Soc.* **2012**, *134*, 836–839.
[55] Y. Jiang, J. Huang, V. R. Reddy Marthala, Y. S. Ooi, J. Weitkamp, M. Hunger, *Microporous Mesoporous Mater.* **2007**, *105*, 132–139.
[56] I. L. C. Buurmans, B. M. Weckhuysen, *Nat. Chem.* **2012**, *4*, 873–886.
[57] E. Runge, E. K. U. Gross, *Phys. Rev. Lett.* **1984**, *52*, 997–1000.
[58] A. Dreuw, M. Head-Gordon, *Chem. Rev.* **2005**, *105*, 4009–4037.
[59] C. Jamorski, M. E. Casida, D. R. Salahub, *J. Chem. Phys.* **1996**, *104*, 5134–5147.
[60] A. Görling, H. H. Heinze, S. P. Ruzankin, M. Staufer, N. Rosch, *J. Chem. Phys.* **1999**, *110*, 2785–2799.
[61] D. Jacquemin, E. A. Perpe, I. Ciofini, C. Adamo, *J. Chem. Theory Comput.* **2010**, *6*, 2071–2085.

[62] T. Stein, L. Kronik, R. Baer, *J. Am. Chem. Soc.* **2009**, *131*, 2818–2820.
[63] L. Goerigk, S. Grimme, *J. Chem. Phys.* **2010**, *132*, 184103.
[64] S. Grimme, M. Parac, *ChemPhysChem* **2003**, *4*, 292–295.
[65] B. M. Wong, T. H. Hsieh, *J. Chem. Theory Comput.* **2010**, *6*, 3704–3712.
[66] R. M. Richard, J. M. Herbert, *J. Chem. Theory Comput.* **2011**, *7*, 1296–1306.
[67] N. Kuritz, T. Stein, R. Baer, L. Kronik, *J. Chem. Theory Comput.* **2011**, *7*, 2408–2415.
[68] L. Goerigk, S. Grimme, *J. Chem. Theory Comput.* **2011**, *7*, 3272–3277.
[69] I. Alata, C. Dedonder, M. Broquier, E. Marceca, C. Jouvet, *J. Am. Chem. Soc.* **2010**, *132*, 17483–17489.
[70] E. Fois, G. Tabacchi, G. Calzaferri, *J. Phys. Chem. C* **2010**, *114*, 10572–10579.
[71] A. R. Leach, *Molecular Modelling: Principles and Applications*, Longman Pub Group, London, **1997**.
[72] V. Barone, J. Bloino, S. Monti, A. Pedone, G. Prampolini, *Phys. Chem. Chem. Phys.* **2010**, *12*, 10550–10561.
[73] V. Barone, J. Bloino, S. Monti, A. Pedone, G. Prampolini, *Phys. Chem. Chem. Phys.* **2011**, *13*, 2160–2166.
[74] L. Palumbo, F. Bonino, P. Beato, M. Bjorgen, A. Zecchina, S. Bordiga, *J. Phys. Chem. C* **2008**, *112*, 9710–9716.
[75] W. Dai, X. Wang, G. Wu, L. Li, N. Guan, M. Hunger, *ChemCatChem* **2012**, *4*, 1428–1435.
[76] W. Dai, M. Scheibe, N. Guan, L. Li, M. Hunger, *ChemCatChem* **2011**, *3*, 1130–1133.
[77] J. Macht, R. T. Carr, E. Iglesia, *J. Am. Chem. Soc.* **2009**, *131*, 6554–6565.
[78] K. Hemelsoet, V. Van Speybroeck, M. Waroquier, *J. Phys. Chem. A* **2008**, *112*, 13566–13573.
[79] K. Hemelsoet, V. Van Speybroeck, M. Waroquier, *ChemPhysChem* **2008**, *9*, 2349–2358.
[80] K. Hemelsoet, F. De Vleeschouwer, V. Van Speybroeck, F. De Proft, P. Geerlings, M. Waroquier, *ChemPhysChem* **2011**, *12*, 1100–1108.
[81] J. R. Platt, *J. Chem. Phys.* **1949**, *17*, 484–496.
[82] M. Parac, S. Grimme, *Chem. Phys.* **2003**, *292*, 11–21.
[83] M. Torrent-Sucarrat, J. M. Anglada, J. M. Luis, *J. Chem. Theory Comput.* **2011**, *7*, 3935–3943.
[84] N. Mohan, K. P. Vijayalakshmi, N. Koga, C. H. Suresh, *J. Comput. Chem.* **2010**, *31*, 2874–2882.
[85] M. Hammonds, A. Pathak, P. J. Sarre, *Phys. Chem. Chem. Phys.* **2009**, *11*, 4458–4464.
[86] L. Karwacki, E. Stavitski, M. H. F. Kox, J. Kornatowski, B. M. Weckhuysen, *Angew. Chem.* **2007**, *119*, 7366–7369; *Angew. Chem. Int. Ed.* **2007**, *46*, 7228–7231.
[87] L. Karwacki, M. H. F. Kox, D. A. M. de Winter, M. R. Drury, J. D. Meeldijk, E. Stavitski, W. Schmidt, M. Mertens, P. Cubillas, N. John, A. Chan, N. Kahn, S. R. Bare, M. Anderson, J. Kornatowski, B. M. Weckhuysen, *Nat. Mater.* **2009**, *8*, 959–965.
[88] E. A. Eilertsen, M. H. Nilsen, R. Wendelbo, U. Olsbye, K. P. Lillerud, *Stud. Surf. Sci. Catal.* **2008**, *174A*, 265–268.
[89] Gaussian 03, Revision E.01, M. J. Frisch, G. W. Trucks, H. B. Schlegel, G. E. Scuseria, M. A. Robb, J. R. Cheeseman, J. J. A. Montgomery, T. Vreven, K. N. Kudin, J. C. Burant, J. M. Millam, S. S. Iyengar, J. Tomasi, V. Barone, B. Mennucci, M. Cossi, G. Scalmani, N. Rega, G. A. Petersson, H. Nakatsuji, M. Hada, M. Ehara, K. Toyota, J. Hasegawa, M. Ishida, T. Nakajima, Y. Honda, O. Kitao, H. Nakai, M. Klene, X. Li, J. E. Knox, H. P. Hratchian, J. B. Cross, V. Bakken, C. Adamo, J. Jaramillo, R. Gomperts, R. E. Stratmann, O. Yazyev, A. J. Austin, R. Cammi, C. Pomelli, J. W. Ochterski, P. Y. Ayala, K. Morokuma, G. A. Voth, P. Salvador, J. J. Dannenberg, V. G. Zakrzewski, S. Dapprich, A. D. Daniels, M. C. Strain, O. Farkas, D. K. Malick, A. D. Rabuck, K. Raghavachari, J. B. Foresman, J. V. Ortiz, Q. Cui, A. G. Baboul, S. Clifford, J. Cioslowski, B. B. Stefanov, G. Liu, A. Liashenko, P. Piskorz, I. Komaromi, R. L. Martin, D. J. Fox, T. Keith, M. A. Al-Laham, C. Y. Peng, A. Nanayakkara, M. Challacombe, P. M. W. Gill, B. Johnson, W. Chen, M. W. Wong, C. Gonzalez, J. A. Pople, Gaussian, Inc., **2004**.
[90] Gaussian 09, Revision A.02, M. J. Frisch, G. W. Trucks, H. B. Schlegel, G. E. Scuseria, M. A. Robb, J. R. Cheeseman, G. Scalmani, V. Barone, B. Mennucci, G. A. Petersson, H. Nakatsuji, M. Caricato, X. Li, H. P. Hratchian, A. F. Izmaylov, J. Bloino, G. Zheng, J. L. Sonnenberg, M. Hada, M. Ehara, K. Toyota, R. Fukuda, J. Hasegawa, M. Ishida, T. Nakajima, Y. Honda, O. Kitao, H. Nakai, T. Vreven, J. A. Montgomery, Jr., J. E. Peralta, F. Ogliaro, M. Bearpark, J. J. Heyd, E. Brothers, K. N. Kudin, V. N. Staroverov, R. Kobayashi, J. Normand, K. Raghavachari, A. Rendell, J. C. Burant, S. S. Iyengar, J. Tomasi, M. Cossi N, Rega, N. J. Millam, M. Klene, J. E. Knox, J. B. Cross, V. Bakken, C. Adamo, J. Jaramillo, R. Gomperts, R. E. Stratmann, O. Yazyev, A. J. Austin, R. Cammi, C. Pomelli, J. W. Ochterski, R. L. Martin, K. Morokuma, V. G. Zakrzewski, G. A. Voth, P. Salvador, J. J. Dannenberg, S. Dapprich, A. D. Daniels, Ö. Farkas, J. B. Foresman, J. V. Ortiz, J. Cioslowski, D. J. Fox, Gaussian, Inc., **2009**.
[91] A. D. Becke, *J. Chem. Phys.* **1993**, *98*, 5648–5652.
[92] C. T. Lee, W. T. Yang, R. G. Parr, *Phys. Rev. B* **1988**, *37*, 785–789.
[93] K. Hemelsoet, A. Nollet, M. Vandichel, D. Lesthaeghe, V. Van Speybroeck, M. Waroquier, *ChemCatChem* **2009**, *1*, 373–378.
[94] K. Hemelsoet, A. Nollet, V. Van Speybroeck, M. Waroquier, *Chem. Eur. J.* **2011**, *17*, 9083–9093.
[95] S. A. Trygubenko, D. J. Wales, *J. Chem. Phys.* **2004**, *120*, 2082–2094.
[96] G. Henkelman, B. P. Uberuaga, H. Jonsson, *J. Chem. Phys.* **2000**, *113*, 9901–9904.
[97] J. Van der Mynsbrugge, K. Hemelsoet, M. Vandichel, M. Waroquier, V. Van Speybroeck, *J. Phys. Chem. C* **2012**, *116*, 5499–5508.
[98] T. Yanai, D. P. Tew, N. C. Handy, *Chem. Phys. Lett.* **2004**, *393*, 51–57.
[99] J. Tomasi, B. Mennucci, R. Cammi, *Chem. Rev.* **2005**, *105*, 2999–3093.
[100] A. V. Marenich, C. J. Cramer, D. G. Truhlar, *J. Phys. Chem. B* **2009**, *113*, 6378–6396.
[101] http://cp2k.berlios.de/.
[102] G. Lippert, J. Hutter, M. Parrinello, *Mol. Phys.* **1997**, *92*, 477–487.
[103] S. Goedecker, M. Teter, J. Hutter, *Phys. Rev. B* **1996**, *54*, 1703–1710.
[104] C. Hartwigsen, S. Goedecker, J. Hutter, *Phys. Rev. B* **1998**, *58*, 3641–3662.
[105] S. Grimme, *J. Comput. Chem.* **2004**, *25*, 1463–1473.
[106] T. Verstraelen, M. Van Houteghem, V. Van Speybroeck, M. Waroquier, *J. Chem. Inf. Model.* **2008**, *48*, 2414–2424.

Received: May 22, 2013
Published online: ■■ ▮▮, 0000

Simulated UV/Vis spectra of a series of (poly)methylated (poly)aromatics representing reaction intermediates of methanol-to-olefins conversion over chabazite catalysts were obtained by a combination of time-dependent density functional theory and ab initio molecular dynamics. The latter was used to take the flexibility of the target molecules into account. The procedure allows a theoretical energy absorption scale to be constructed and absorption bands observed in in situ UV/Vis spectra to be assigned to structurally different species (see figure).

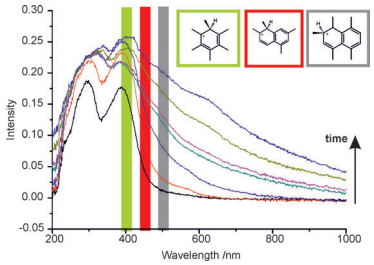

Heterogeneous Catalysis

K. Hemelsoet, Q. Qian, T. De Meyer, K. De Wispelaere, B. De Sterck, B. M. Weckhuysen, M. Waroquier, V. Van Speybroeck* ..... ▮▮▮▮–▮▮▮▮*

Identification of Intermediates in Zeolite-Catalyzed Reactions by In Situ UV/Vis Microspectroscopy and a Complementary Set of Molecular Simulations